Wave Height Estimation From X-Band Nautical Radar Images Using Temporal Convolutional Network

Weimin Huang, *Senior Member, IEEE*, Zhiding Yang, *Student Member, IEEE*, and Xinwei Chen, *Student Member, IEEE*

***Abstract*—In this article, a temporal convolutional network (TCN)-based model is proposed to retrieve significant wave height (H_s) from X-band nautical radar images. Three types of features are first extracted from radar image sequences based on signal-to-noise ratio (SNR), ensemble empirical mode decomposition (EEMD), and gray level cooccurrence matrix methods, respectively. Then, feature vectors are input into the proposed TCN-based regression model to produce H_s estimation. Radar data are collected from a moving vessel at the East Coast of Canada, as well as the simultaneous wave data measured by several wave buoys deployed nearby are used for model training and testing. Experimental results after averaging show that TCN-based model further improves the H_s estimation accuracy, with reductions of root-mean-square errors by 0.33 and 0.10 m, respectively, compared to the SNR-based and the EEMD-based linear fitting methods. It has also been found that under the same feature extraction scheme, TCN outperforms other machine learning-based algorithms including support vector regression and the gated recurrent unit network.**

***Index Terms*—Significant wave height (H_s), temporal convolutional network (TCN), X-band nautical radar.**

I. Introduction

ACCURATE measurement of sea surface wave parameters, especially the significant wave height (H_s), is critical for a variety of maritime applications, such as offshore wind farm development, oil and gas exploitation, ship navigation, breakwater construction, and cross-sea bridge building [1]. Traditionally, *in situ* sensors such as wave buoys are employed for wave measurements. However, they only provide H_s data at the current position of interest [2]. In contrast, radar sensors are able to explore and measure H_s within a much wider area. Among different types of radars sensors, the nautical X-band radar is a favorable choice for real-time wave estimation due to its high temporal and spatial resolution. Besides, it can be mounted at different locations including moving ships, fixed offshore platforms, and nautical traffic control towers with relatively low cost for deployment and maintenance [3].

The Bragg resonance interactions between the X-band electromagnetic waves and the cm-scale capillary waves induced by local winds generate the radar backscatter from the sea surface [4]. The base signal (short waves) is then modulated by longer ocean waves under multiple mechanisms such as hydrodynamic effects, tilt modulation, and shadowing effects [1]. After modulation, longer sea surface waves become visible in radar backscatter (i.e., sea clutter) images, which are manifested by strip-like patterns. During the past several decades, different methods have been proposed for estimating H_s from X-band radar images. One of the most popular methods is the signal-to-noise ratio (SNR)-analysis-based method proposed by Nieto-Borge *et al.* [5]. Although it has been incorporated into several commercial radar systems for real-time wave monitoring, later studies have found that H_s is not completely linearly proportional to the square root of SNR because of the effect of the variations of sea states, the differences of SNR calculation methods, as well as radar systems [2], [6], [7]. Later, several other spectral analysis-based algorithms are presented for wave height estimation, including the iterative least squares-based algorithms [8], the adaptive recursive positioning method-based algorithms [9], the 2D continuous wavelet transform-based algorithms [10], and the array-beamforming-based algorithms [11]. On the other hand, H_s can be determined by analyzing the texture of radar images, relevant methods include illumination-probability-based method [12], statistical-analysis-based method [13], tilt-based algorithm [14], shadowing-based algorithms [15], empirical orthogonal function-based methods [16] and ensemble empirical mode decomposition (EEMD)-based algorithms [7]. Furthermore, it should be noted that in recent years, machine learning (ML)-based algorithms have been increasingly incorporated into wave height estimation models, such as artificial neural network (ANN), [2], [17]–[19], support vector regression (SVR) [20], [21], convolutional neural network (CNN) [22], and convolutional gated recurrent unit network (CGRU) [3]. The SVR-based methods proposed in [20] and [21] and the ANN-based method proposed in [17] use square root of SNR as the main feature to train the estimation model. However, it is found that more effective features need to be combined for analysis to improve the estimation accuracy [2]. Besides, although the CNN-based and CGRU-based methods are end-to-end systems that learn to

Manuscript received August 17, 2021; revised October 19, 2021; accepted October 30, 2021. Date of publication November 4, 2021; date of current version November 18, 2021. The work of W. Huang was supported by the Natural Sciences and Engineering Research Council of Canada Discovery Grants under Grant NSERC RGPIN-2017-04508 and Grant RGPAS-2017-507962. *(Corresponding author: Weimin Huang.)*

The authors are with the Faculty of Engineering and Applied Science, Memorial University of Newfoundland, St. John's, NL A1B 3X5, Canada (e-mail: weimin@mun.ca; zhidingy@mun.ca; xinweic@mun.ca).

Digital Object Identifier 10.1109/JSTARS.2021.3124969

TABLE I
RADAR INFORMATION

Transmit frequency	9.41 GHz
Polarization	Horizontal
Pulse width	50 ns
Range resolution	7.5 m
Range coverage	240 m - 2160 m
Beam width	2°
Azimuth coverage	360°
Antenna height	21.9 m
Antenna rotation speed	28 rpm
Grey level of radar image	0 - 255

extract features automatically, it is hard to analyze the relationship between those highly abstract features and H_s. In our recent works, ML-based methods have been developed to estimate wave direction and period using radar images. Therefore, this article will focus on the development of ML-based algorithms for H_s estimation. Among different types of neural networks, temporal convolutional network (TCN) is a variant of CNN architecture for sequence network modeling proposed in [23]. Compared to other typical CNNs, TCN-based estimation model can exhibit longer effective memory, which indicates that H_s can be analyzed in conjunction with more long-term data. Thus, H_s can not only be estimated from the spatial features extracted from the current radar image but also the temporal variations exploited from preceding radar image sequence.

In this article, a TCN-based H_s estimation model that employs three types of H_s-related input features is proposed. In Section II, the radar and wave data used in this study are introduced. The procedures of feature extraction and the architecture of TCN are described in Section III. Section IV illustrates the experimental results and comparisons among different ML-based algorithms. Finally, Section V concludes this article.

II. DATA OVERVIEW

The radar data used in this study were collected by an X-band nautical radar (Decca) operating at grazing incidence with horizontal transmit and horizontal receive (HH) polarization. The radar system was installed on a moving vessel and its information is provided in Table I. During the data collection periods (from November 26 to December 4, 2008), the vessel was moving around 300-km south-southeast of Halifax, Nova Scotia, Canada, where the water depth is around 200 m. Each radar image sequence data file is generated every 2 min by wave monitoring system (WaMoS II), which produces images in gray levels (from 0 to 255). Since the antenna rotation period is around 2.5 s, each sequence file includes 32 radar images in time series. The original radar images are presented in polar coordinate and can be transformed into Cartesian coordinate through scan conversion. It should be noted that the presence of rain may blur wave signatures and lead to inaccurate wave estimation [24], [25], data collected under rainfall conditions are excluded from the analysis. Simultaneous wave measurements from three Triaxys directional wave buoys that were deployed in a drifting mode [26] are used as ground truths for model training, validation, and testing purposes. In order to keep a short distance

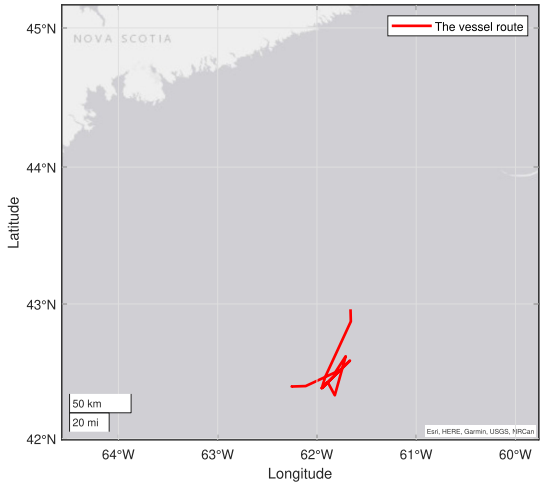

Fig. 1. Route of the vessel during radar data collection periods.

from the drifting buoys, the vessel sailed or moored near the buoys during the data collection period. The distances between the vessel and the buoys are generally less than 10 km. Besides, the route of the vessel is shown in red lines of Fig. 1. Those buoys are able to measure H_s ranging from 0 to 20 m with a resolution of 0.01 m, and an error within 2%. Since the reference H_s was measured around every 30 min, the simultaneous H_s for each radar image sequence can be obtained by temporal averaging and interpolation.

III. METHODOLOGY

A. Feature Extraction

In this study, three types of features are extracted using different algorithms and combined as the input feature vector for the estimation model, which are introduced as follows.

1) SNR Feature Extraction: In [5], SNR was calculated from radar-derived wave spectrum based on 3D Fourier transform analysis and it used to determine H_s through linear regression. Here, a series of 32 Cartesian radar images contained in each file are used to generate one estimation result. For each radar image, a 128 × 128 subimage centered at the upwind direction is selected, as shown in Fig. 2. The calculation of SNR involves several steps. First, the image spectrum of the selected region $F_I(\boldsymbol{k}, \omega)$ is obtained by applying the 3D Fourier transform [4], where $\boldsymbol{k} = (k_x, k_y)$ is the two-dimensional wave number vector and ω is the angular frequency of the ocean wave. According to the linear gravity wave theory [4], [27], the dispersion relation can be expressed as

$$\omega = \sqrt{g|\boldsymbol{k}| \tanh(|\boldsymbol{k}|d)} + \boldsymbol{k} \cdot \boldsymbol{U} \tag{1}$$

where d is the water depth, g is the gravitational acceleration, and $\boldsymbol{U} = (U_x, U_y)$ is the velocity of encounter (i.e., combination of the velocities of radar platform and current) [27], [28]. Then, $\boldsymbol{U}$ can be determined by a least square analysis method using the dispersion relation (1) according to the image spectrum [4], [29]. Besides, the high harmonic dispersion relation is also

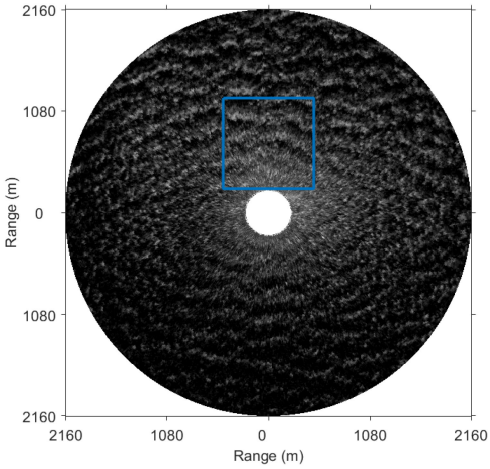

Fig. 2. Selected subimage (outlined in blue) for calculating SNR.

considered, which can be expressed as

$$\omega_q = (q+1)\sqrt{\frac{g|\boldsymbol{k}|}{q+1}\tanh\left(\frac{|\boldsymbol{k}|d}{q+1}\right)} + \boldsymbol{k}\cdot\boldsymbol{U} \tag{2}$$

where q represents the order of the qth-harmonic. The main spectral components of the image spectrum include the wave-related component, high harmonics caused by shadowing modulation, and background spectral noise (BGN) due to the roughness caused by the local wind on the sea surface [30]. The wave-related image spectrum (denoted as $F_F(\boldsymbol{k},\omega)$) can be extracted from $F_I(\boldsymbol{k},\omega)$ by applying a filter based on the linear wave dispersion relationship (1). Hence, those components in the image spectrum that do not belong to wave field can be filtered [4]. Similarly, the high harmonic spectrum (denoted as $F_H(\boldsymbol{k},\omega)$) also can be obtained from $F_I(\boldsymbol{k},\omega)$ (2).

Thus, the 3D BGN spectrum (denoted as $F_{\text{BGN}}(\boldsymbol{k},\omega)$) can be approximated as

$$F_{\text{BGN}}(\boldsymbol{k},\omega) \simeq F_I(\boldsymbol{k},\omega) - F_F(\boldsymbol{k},\omega) - F_H(\boldsymbol{k},\omega). \tag{3}$$

Next, due to the nonlinearity of radar imaging process, the wave spectrum (denoted as $F_W(\boldsymbol{k},\omega)$) is estimated from $F_F(\boldsymbol{k},\omega)$ using an empirical modulation transfer function (MTF, denoted as $T_M(\boldsymbol{k})$) as

$$F_W(\boldsymbol{k},\omega) = F_F(\boldsymbol{k},\omega)\cdot T_M(\boldsymbol{k}). \tag{4}$$

The MTF ($T_M(\boldsymbol{k})$) is expressed as

$$T_M(\boldsymbol{k}) = |\boldsymbol{k}|^{\beta} \tag{5}$$

where β is the MTF exponent, which is empirically suggested as 1.2 [31]. Finally, the SNR can be obtained as the ratio of the integration of the wave spectrum and the integration of BGN as

$$\text{SNR} = \frac{\int \text{F}_{\text{W}}(\boldsymbol{k},\omega)\text{d}^2\text{k}\text{d}\omega}{\int \text{F}_{\text{BGN}}(\boldsymbol{k},\omega)\text{d}^2\text{k}\text{d}\omega}. \tag{6}$$

Finally, the calculated $\sqrt{\text{SNR}}$ is considered as the SNR feature that is input into the network model.

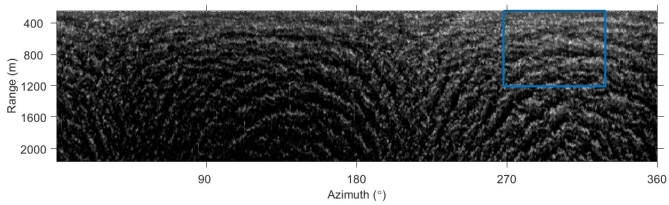

Fig. 3. Selected subimage (outlined in blue) for EEMD-based feature extraction.

2) EEMD Feature Extraction: Before this feature extraction, a subimage ranging from 240 to 1200 m to radar site and ±30○ around the upwind direction is selected from the first polar radar image in each sequence file, as displayed in Fig. 3. The details of feature extraction are illustrated as follows. First, the subimage can be represented by I_{sub} as

$$I_{\text{sub}} = \begin{bmatrix} p_{(1,1)} & p_{(1,2)} & \cdots & p_{(1,N)} \\ p_{(2,1)} & p_{(2,2)} & \cdots & p_{(1,N)} \\ \vdots & \vdots & \ddots & \vdots \\ p_{(M,1)} & p_{(M,2)} & \cdots & p_{(M,N)} \end{bmatrix}. \tag{7}$$

Then, EEMD is applied to each column (azimuthal direction) of I_{sub} to obtain the first five intrinsic mode functions (IMFs) and a residual term, which can be obtained as

$$I_{\text{sub}}(\sim,n) = \sum_{j=1}^{5} C_j(\sim,n) + R(\sim,n) \tag{8}$$

where n is the nth column of the subimage. Each IMF can be split into the amplitude modulation (AM, denoted as A) and frequency modulation (FM, denoted as F) portions [32] using the normalization scheme, where the AM part $A_j(\sim,n)$ is expressed as

$$A_j(\sim,n) = \begin{bmatrix} a_{1,n,j} \\ a_{2,n,j} \\ \vdots \\ a_{M,n,j} \end{bmatrix}. \tag{9}$$

Eventually, the AM portions of the 2nd–5th IMFs are calculated and averaged in each azimuth and range of the subimage, which can be expressed as

$$S = \frac{1}{N}\frac{1}{M}\sum_{j=2}^{5} A_j. \tag{10}$$

In [7], the calculated average (S) is used to estimate H_s with linear regression. Here, it is employed as another input of the network model.

3) Gray Level Cooccurrence Matrix (GLCM) Feature Extraction: Since GLCM analysis has already been employed for retrieving wave direction and wave period [33], it is reasonable to further analyze GLCM-based features for H_s estimation. The selected region for feature extraction is the same as the region extracted for the EEMD feature. A 29×29 sliding window is first applied to the subimage. The distance between the pixel pairs in each sliding window is set as 4, while the positional

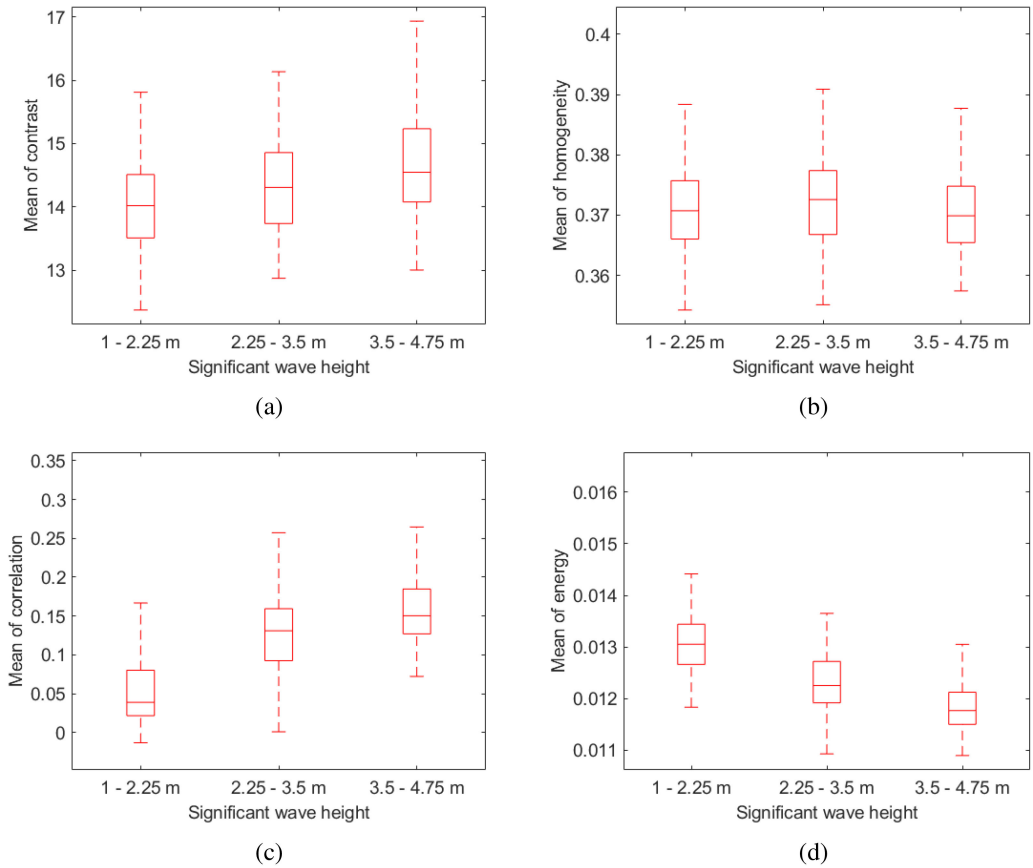

Fig. 4. Median value distribution of mean. (a) Contrast. (b) Homogeneity. (c) Correlation. (d) Energy.

relationships of pixel pairs are in four directions (0°, 45°, 90°, and 135°) [34]. In this study, four statistics calculated from each GLCM, i.e., contrast (Con), homogeneity (H), correlation (Cor), and energy (E) are selected. In order to verify the influence of different H_s on the GLCM feature values, the median values of mean and standard deviation of four features over four directions from all sliding windows in each radar subimage are calculated and compared under different H_s ranges (1.00–2.25, 2.25–3.50, 3.50–4.75 m), as shown in the box plots in Figs. 4 and 5. It can be observed that only two out of the eight figures (i.e., the median values of mean contrast and mean homogeneity) do not show clear correlations with H_s. Thus, metrics presented in the other six figures are selected from each radar image for H_s estimation, i.e.,

1) median of mean correlation;
2) median of mean energy;
3) median of contrast standard deviation;
4) median of homogeneity standard deviation;
5) median of correlation standard deviation; and
6) median of energy standard deviation.

Those six features are combined with the SNR and EEMD features to form a feature vector. Then, the combined feature vector is normalized by using zero-center normalization. Assume that the collection of each type of features extracted from all sequences is denoted as T, the normalization operation results in

$$T_{\text{norm}} = \frac{T - \text{mean}(T)}{\text{std}(T)} \tag{11}$$

where T_{norm} is the collection of each type of normalized features, $\text{mean}(T)$ and $\text{std}(T)$ are the mean value and standard deviation of each type of feature collection in all sequences. Finally, a total of eight normalized features are combined as eight-dimensional (8D) feature vector for each input sample in the TCN-based model.

B. TCN-Based Wave Height Estimation Model

TCN is a variant of CNN that convolves over the time domain. The complete architecture of the proposed TCN-based H_s estimation model is presented in Fig. 6, which includes six dilated causal convolution (DCC) layers and a fully connected layer. The functions of each component and operation in the network are briefly introduced as follows.

1) DCC Layer: The visualization of dilated convolution inside six DCC layers is shown in Fig. 7. It can be observed that the outputs of each convolution layer are calculated only from its current and earlier input samples. On the other hand, it also allows interval sampling of the input during convolution, which allows larger effective history inputs without pooling

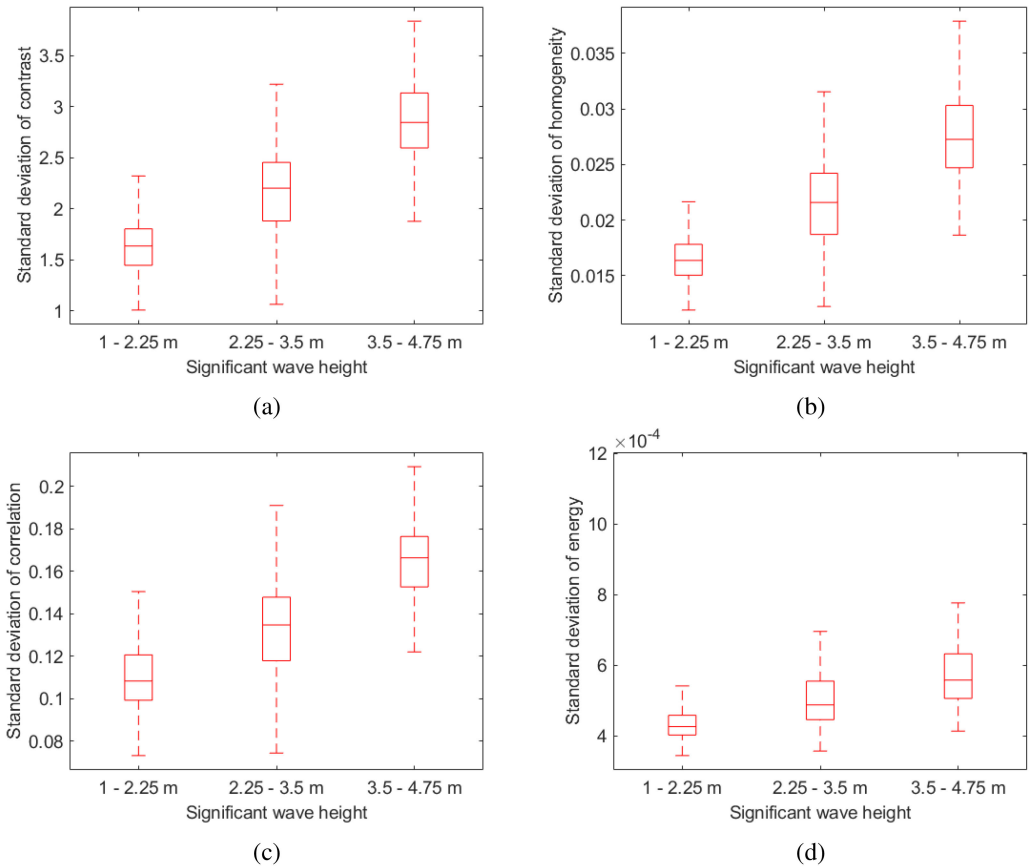

Fig. 5. Median value distribution of standard deviation. (a) Contrast. (b) Homogeneity. (c) Correlation. (d) Energy.

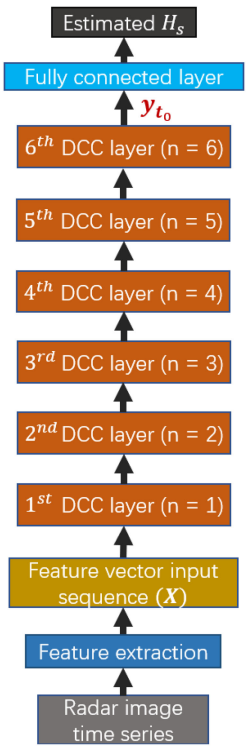

Fig. 6. Overall framework of the TCN-based H_s estimation model.

operation [35]. As shown in Fig. 7, the sampling rate is controlled by the dilation factor, which increases exponentially with the depth of the network. For the nth DCC layer, the dilation factor is given by $d_n = 2^{(n-1)}, n \in \{1, 2, \ldots, 6\}$. Besides, the filter size in each convolution operation is $k \times 1$, where k is equal to 3 in this study. The number (r) of input samples in the receptive field of this network is determined by d_n and k, resulting in

$$r = 1 + \sum_{n=1}^{6} (k-1) \times d_n = 127. \tag{12}$$

As mentioned above, each sample in the input sequences ($\boldsymbol{X}$) consists of an 8D feature vector. In order to estimate H_s of a certain time (t_0) in the sequences, a total of 127 8D feature vectors ($\boldsymbol{x}_{t_0}, \boldsymbol{x}_{t_0-1}, \ldots, \boldsymbol{x}_{t_0-126}$) are extracted as the receptive field to produce an 8D result ($\boldsymbol{y}_{t_0}$) from 6 DCC layers.

The detailed calculation steps in each DCC layer are illustrated in Fig. 8, which include convolution operation, rectified linear unit (ReLU), and dropout. A total of eight filters are used in each convolution operation. In particular, all elements in eight filters can be denoted as $f_{ij}, i \in \{1, 2, 3, 4, 5, 6, 7, 8\}, j \in \{1, 2, 3\}$, where i represents the index of filters and j represents the index of elements in the ith filter. The values of each filter are initialized with normal distribution. As displayed in Fig. 9, the collections of f_{i1}, f_{i2}, and $f_{i3}, i \in \{1, 2, 3, 4, 5, 6, 7, 8\}$ are,

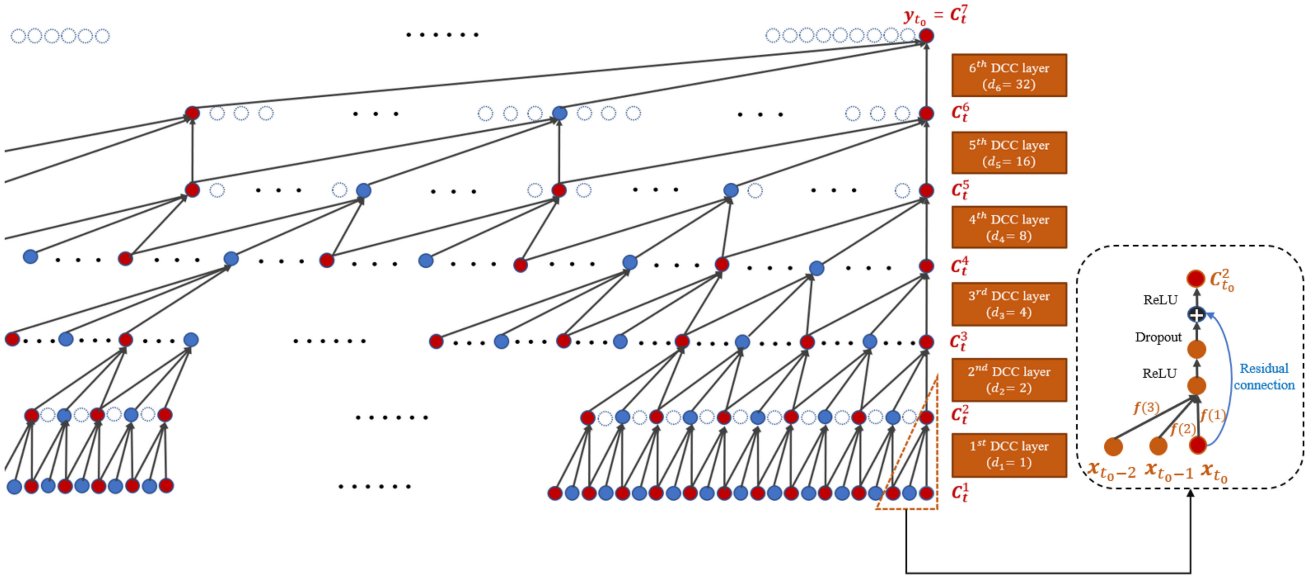

Fig. 7. Visualization of dilated convolution in six DCC layers.

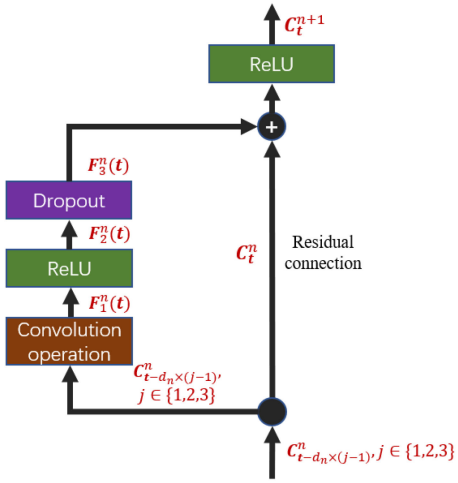

Fig. 8. Structure of each DCC layer.

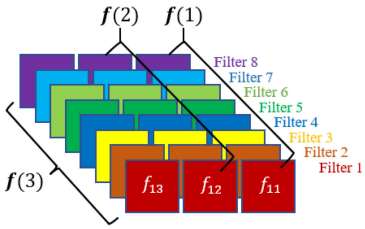

Fig. 9. Figure illustration of 8 3×1 filters used in the convolution operation.

respectively, denoted as three 8D vectors $\boldsymbol{f}(1)$, $\boldsymbol{f}(2)$, and $\boldsymbol{f}(3)$ for the convolution operation. In Fig. 7, $\boldsymbol{C}_t^n$ indicates the input of convolution operation at time $\boldsymbol{t}$ in the nth DCC layer, which is marked in red. Due to the dilation, $\boldsymbol{t}$ of each input sample used

TABLE II
RMSE COMPARISON OF ESTIMATED H_s FOR DIFFERENT INPUT FEATURES

Input features	RMSEs of estimated H_s using TCN		
	Training	Validation	Testing
SNR	0.67 m	0.57 m	0.58 m
EEMD	0.42 m	0.41 m	0.41 m
GLCM	0.34 m	0.39 m	0.41 m
SNR +EEMD	0.42 m	0.38 m	0.39 m
SNR +GLCM	0.30 m	0.37 m	0.38 m
EEMD+GLCM	0.29 m	0.36 m	0.35 m
SNR + EEMD+GLCM	0.26 m	0.32 m	0.32 m

in the nth DCC layer can be expressed as

$$\boldsymbol{t} = t_0 - 2^n \times l, l \in \{0, 1, \ldots, 2^{7-n} - 2\}. \tag{13}$$

Therefore, the output of convolution operation at time $\boldsymbol{t}$ in the nth DCC layer can be expressed as

$$\boldsymbol{F}_1^n(\boldsymbol{t}) = \sum_{j=1}^{3} \boldsymbol{f}(j) * \boldsymbol{C}_{\boldsymbol{t}-d_n\times(j-1)}^n \tag{14}$$

where $*$ denotes element-wise product. When $n = 1$, the inputs can be given as $\boldsymbol{C}_{\boldsymbol{t}-d_1\times(j-1)}^1 = \boldsymbol{x}_{\boldsymbol{t}-d_1\times(j-1)}$.

Then, the convolution operation is followed by ReLU. ReLU is a kind of activation function [36] that sets all negative input values to zero in order to achieve nonlinear transformation of the data, which is given by

$$\boldsymbol{F}_2^n(\boldsymbol{t}) = \mathrm{ReLU}(\boldsymbol{F}_1^n(\boldsymbol{t})). \tag{15}$$

Compared to other activation functions, ReLU further reduces computation by adding more sparsity.

In order to prevent overfitting, the dropout operation is used as a form of regularization after ReLU [37], which will probabilistically drop out nodes in the network during the training. Assuming that output values in ReLU operation are kept for futher computation with a probability of p, the expression can

TABLE III
COMPARISONS OF RESULTS USING DIFFERENT METHODS FOR H_s ESTIMATION

	Training			Validation			Testing (without averaging)			Testing (with averaging)		
	RMSE	CC	Bias	RMSE	CC	Bias	RMSE	CC	Bias	RMSE	CC	Bias
SNR-based linear fitting method	0.68 m	0.59	-0.01 m	–	–	–	0.59 m	0.62	0.11 m	0.57 m	0.65	0.11 m
EEMD-based linear fitting method	0.44 m	0.86	0 m	–	–	–	0.41 m	0.84	0.07 m	0.34 m	0.90	0.07 m
SVR-based method	0.28 m	0.94	-0.03 m	0.33 m	0.89	-0.06 m	0.32 m	0.89	0.07 m	0.25 m	0.94	0.07 m
GRU-based method	0.28 m	0.95	-0.02 m	0.34 m	0.90	-0.06 m	0.33 m	0.90	0.10 m	0.27 m	0.93	0.10 m
Proposed TCN-based method	0.26 m	0.95	0.04 m	0.32 m	0.91	0.02 m	0.32 m	0.90	0.07 m	0.24 m	0.94	0.07 m

be presented as

$$\boldsymbol{F}_3^n(\boldsymbol{t}) = \boldsymbol{M} * \boldsymbol{F}_2^n(\boldsymbol{t}) \tag{16}$$

where $\boldsymbol{M}$ is the 8D vector consisting of 0 and 1, which is generated by Bernoulli function

$$\boldsymbol{M} \sim \text{Bernoulli}(p). \tag{17}$$

In the proposed model, the probability p is set as 50% in each dropout operation, which means half of the randomly selected output values will be kept while the other half are discarded.

Furthermore, the residual connection [38] is incorporated into the training of deep layers in order to avoid the issue of exploding or vanishing gradients. Specifically, the input of each convolution operation at time $\boldsymbol{t}$ is connected to the output from the dropout operation for the addition operation [23]. Then, ReLU operation is implemented after addition operation. The output ($\boldsymbol{C}_{\boldsymbol{t}}^{n+1}$) can be expressed as

$$\boldsymbol{C}_{\boldsymbol{t}}^{n+1} = \text{ReLU}(\boldsymbol{F}_3^n(\boldsymbol{t}) + \boldsymbol{C}_{\boldsymbol{t}}^n). \tag{18}$$

When $n \leq 5$, $\boldsymbol{C}_{\boldsymbol{t}}^{n+1}$ is considered as the input at time $\boldsymbol{t}$ of next layer. When $n = 6$, $\boldsymbol{t}$ is equal to t_0. Thus, $\boldsymbol{C}_{\boldsymbol{t}}^{6+1}$ can also be written as $\boldsymbol{y}_{t_0}$.

2) Fully Connected Layer: The purpose of this step is to establish the mapping relationship between the 8D output ($\boldsymbol{y}_{t_0}$) from six DCC layers and the final estimated wave height (H_{est}). Assume that $\boldsymbol{y}_{t_0} = (y_1, y_2, \ldots, y_8)$, H_{est} can be obtained as

$$H_{est} = \sum_{i=1}^{8} (w_i y_i + b_i) \tag{19}$$

where w_i and b_i are the updated weight value and bias corresponding to y_i by the Adam algorithm [39].

IV. EXPERIMENTAL RESULTS

A. Model Training

Since data collections were interrupted due to system failure for some periods, and the radar data collected under rain condition are also excluded, a total of 1448 radar image sequences are utilized in this study. 50% of radar image sequences collected in three time periods are used for model training, while the other half are used for testing the estimation accuracy. Fivefold cross validation is applied to the training set. As for the model training, the size of mini-batch and the number of epochs are set to be 64 and 150, respectively.

B. Input Features Validity Analysis

Table II shows the root-mean-square errors (RMSEs) of H_s estimated from the testing samples. In order to validate the effectiveness of the extracted features (SNR, EEMD, and GLCM feature) in wave height estimation, different feature combinations are input to the TCN model for H_s estimation analysis. It can be noticed that the regression accuracy is not satisfactory when only SNR feature is used as the input feature for the network, while the regression result is better when EEMD or GLCM is selected as the single input. When selecting two of the three features, it is noticed that results obtained from the combination with GLCM feature can generate better result than that of the combinations without GLCM feature. It can be observed that when SNR feature is added to the combined features of EEMD and GLCM, the performance of H_s estimation can be further improved and produce the minimum RMSE.

C. Comparisons With Different Methods

In order to compare the performance of TCN-based model with existing methods, the typical SNR-based [5] and EEMD-based [7] linear fitting methods are also implemented to the radar data for estimating H_s. Besides, the SVR-based [40] and gated recurrent unit network (GRU)-based models [41] with the same input features as the TCN model are also employed for comparison. The RMSEs, correlation coefficients (CCs), and biases between the radar-derived H_s of different methods as well as buoy-measured H_s are summarized in Table III. The temporal moving average is applied to the estimated H_s obtained during each time interval between two consecutive buoy measurements. The estimation results from the testing samples with SNR-based linear fitting, EEMD-based linear fitting, SVR-based, GRU-based, and the proposed TCN-based methods before and after moving average are presented in Figs. 10(a)–(e), respectively. In addition, Fig. 11 shows the estimated H_s of all samples before and after moving average in time series.

It can be observed from Table III that compared to the typical SNR-based and EEMD-based linear fitting methods, the proposed method decreases the RMSE by 0.27 and 0.09 m with CC being furthered improved to 0.90. It can be noticed

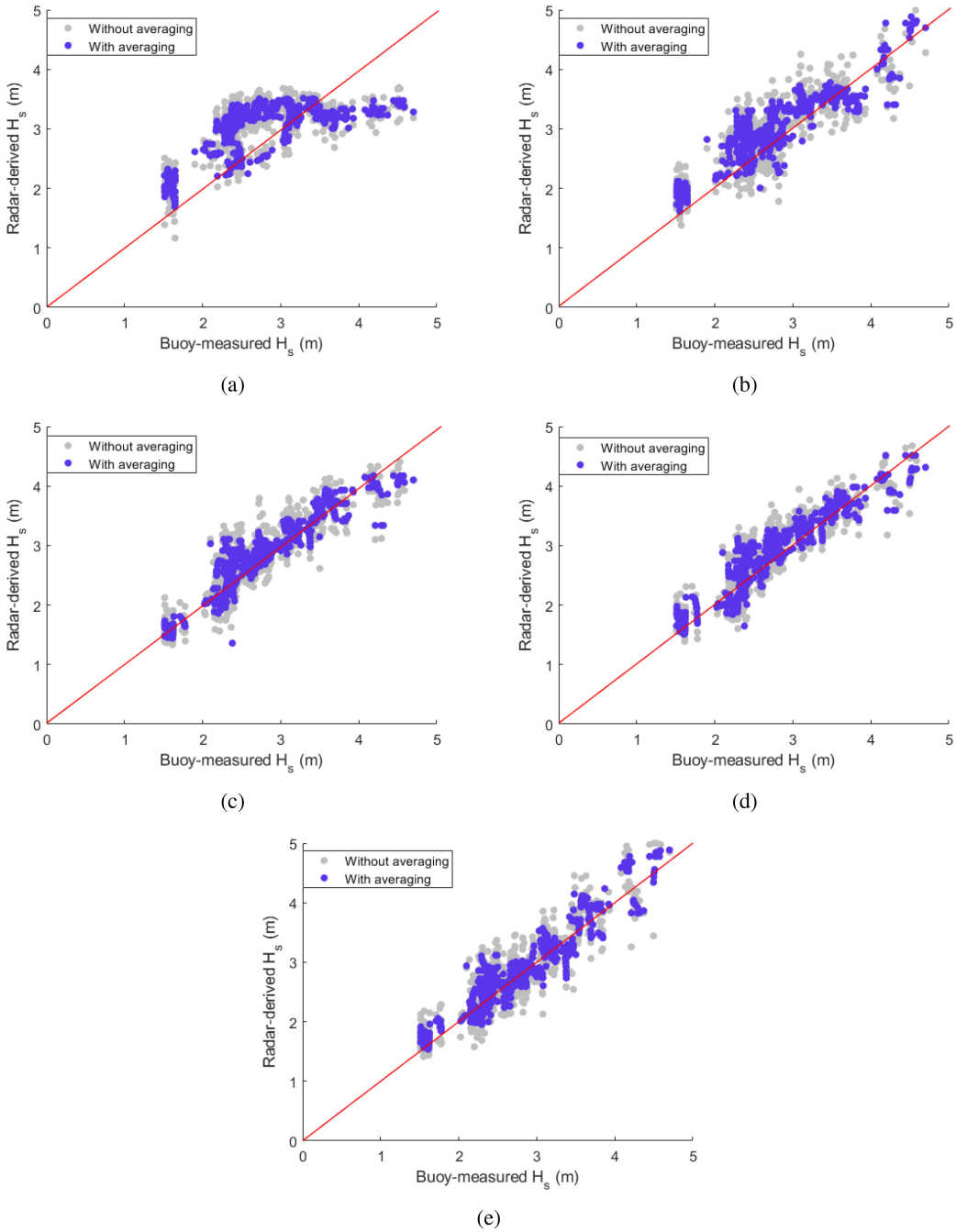

Fig. 10. Scatter plots of buoy-measured H_s and radar-derived H_s with and without temporal moving average. (a)–(e) correspond to SNR-based linear fitting, EEMD-based linear fitting, SVR-based and GRU-based, and the proposed TCN-based methods, respectively.

from Figs. 10(a) and 11(a) that SNR-based linear fitting method cannot present a clearly linear relationship between the square root of SNR and H_s. Specifically, H_s is generally overestimated when the buoy-measured H_s is lower than 3 m and mostly underestimated for higher H_s. Figs. 10(b) and 11(b) show that for EEMD-based method, H_s will be overestimated for buoy-measured H_s lower than 3.5 m. In contrast, the proposed TCN-based method is able to estimate H_s without significant bias. On the other hand, when comparing the estimation results with the other two ML-based methods, it can be observed that while the TCN model still generates the best regression result, the difference is not significant, which indicates that the ML-based methods are more superior to methods that are based on linear regression. Finally, it can be found that when the moving average is applied, the estimation accuracy can be further improved. In particular, the RMSE calculated from the TCN model can decrease to 0.24 m with CC further improved to 0.94.

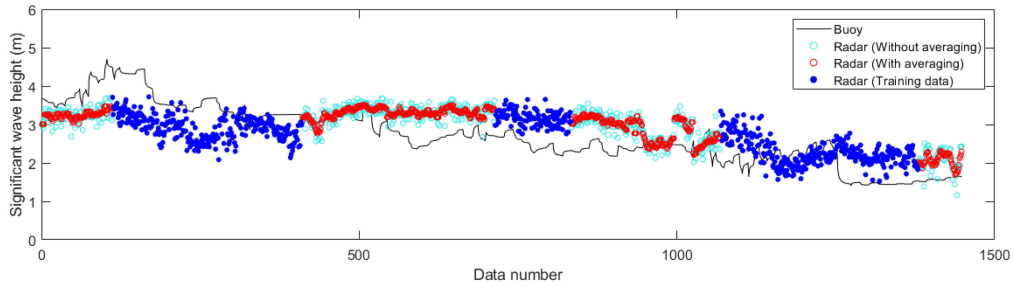

(a)

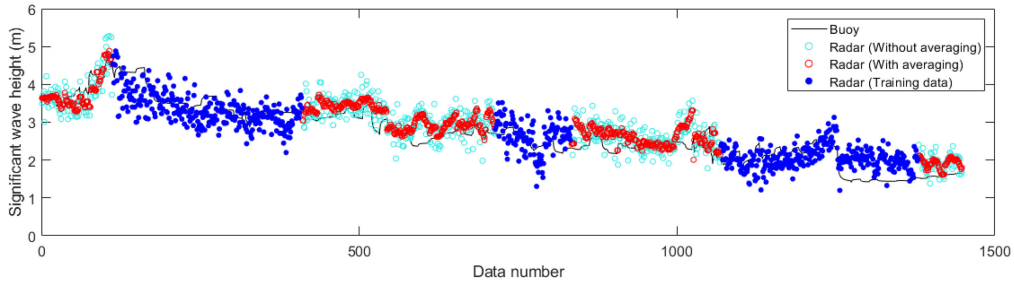

(b)

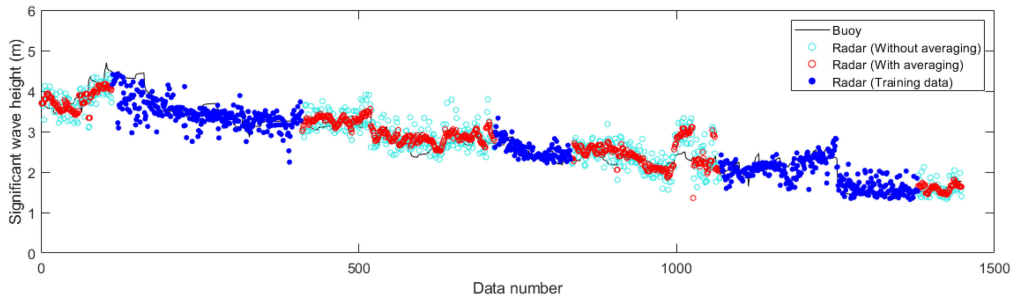

(c)

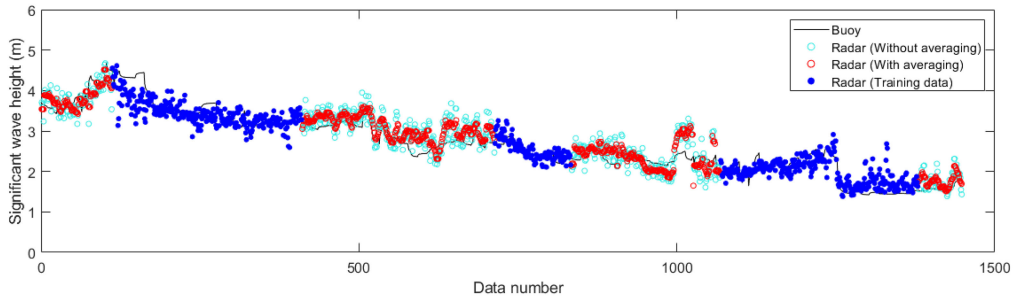

(d)

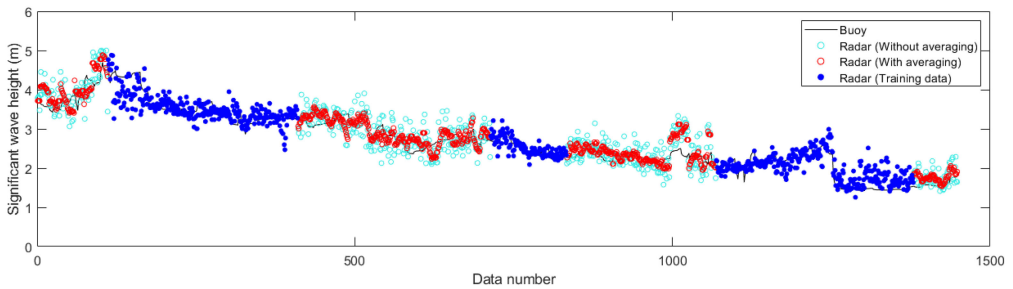

(e)

Fig. 11. H_s estimation results in time series using different methods. Cyan and red scatters represent testing samples without and with temporal averaging, respectively. (a)–(e) correspond to SNR-based linear fitting, EEMD-based linear fitting, SVR-based and GRU-based, and the proposed TCN-based methods, respectively.

V. Conclusion

In this article, the combined features are extracted from X-band radar image sequences to estimate H_s using a TCN-based regression model, which can derive the wave height by combining of spatial and temporal features of radar image sequences. The normalized features calculated by SNR-, EEMD-, and GLCM-based methods are incorporated as the input feature vector for the sequence. Experiment results from the nautical radar data collected from a moving vessel at the East Coast of Canada verified that the combination of all three types of features will generate the best estimation accuracy. On the other hand, the application of moving average can effectively further improve the estimation accuracy. The proposed TCN-based method is also compared with two existing methods. It is found that compared to the typical SNR-based and EEMD-based linear fitting methods, the TCN-based model reduces the RMSEs from 0.57 and 0.34 m to 0.24 m. Moreover, while other ML-based methods such as SVR and GRU can also produce good results, TCN is still the most accurate one. In the future, more image data collected from different radar systems and installation locations should be incorporated into the network to further improve the model's accuracy and robustness. Furthermore, more advanced network architectures for H_s estimation should be explored. Moreover, the evaluation and mitigation of rain effect on H_s should be investigated as well.

Acknowledgment

The authors would like to thank Dr. E. Thornhill from DRDC for the provision of the radar and buoy data.

References

[1] W. Huang, X. Liu, and E. Gill, "Ocean wind and wave measurements using X-band marine radar: A comprehensive review," *Remote Sens.*, vol. 9, no. 12, 2017, Art. no. 1261.

[2] L.-C. Wu, D.-J. Doong, and J.-W. Lai, "Influences of nononshore winds on significant wave height estimations using coastal X-band radar images," *IEEE Trans. Geosci. Remote Sens.*, to be published, doi: 10.1109/TGRS.2021.3077903.

[3] X. Chen and W. Huang, "Spatial-temporal convolutional gated recurrent unit network for significant wave height estimation from shipborne marine radar data," *IEEE Trans. Geosci. Remote Sens.*, to be published, 2021, doi: 10.1109/TGRS.2021.3074075.

[4] I. R. Young, W. Rosenthal, and F. Ziemer, "A three-dimensional analysis of marine radar images for the determination of ocean wave directionality and surface currents," *J. Geophys. Res.-Oceans*, vol. 90, no. C1, pp. 1049–1059, 1985.

[5] J. C. Nieto-Borge, K. Hessner, and P. Jarabo-Amores, "Signal-to-noise ratio analysis to estimate ocean wave heights from X-band marine radar image time series," *IET Radar, Sonar Navigation*, vol. 2, no. 1, pp. 35–41, 2008.

[6] Y. Wei, Z. Lu, G. Pian, and H. Liu, "Wave height estimation from shadowing based on the acquired X-band marine radar images in coastal area," *Remote Sens.*, vol. 9, no. 8, 2017, Art. no. 859.

[7] X. Liu, W. Huang, and E. W. Gill, "Estimation of significant wave height from X-band marine radar images based on ensemble empirical mode decomposition," *IEEE Geosci. Remote. Sens. Lett.*, vol. 14, no. 10, pp. 1740–1744, Oct. 2017.

[8] W. Huang, E. Gill, and J. An, "Iterative least-squares-based wave measurement using X-band nautical radar," *IET Radar, Sonar Navigation*, vol. 8, no. 8, pp. 853–863, 2014.

[9] A. Al-Habashneh, C. Moloney, E. Gill, and W. Huang, "An adaptive method of wave spectrum estimation using X-band nautical radar," *Remote Sens.*, vol. 7, no. 12, pp. 16537–16554, 2015.

[10] J. An, W. Huang, and E. W. Gill, "A self-adaptive wavelet-based algorithm for wave measurement using nautical radar," *IEEE Trans. Geosci. Remote Sens.*, vol. 53, no. 1, pp. 567–577, Jan. 2015.

[11] K. Ma, X. Wu, X. Yue, L. Wang, and J. Liu, "Array beamforming algorithm for estimating waves and currents from marine X-band radar image sequences," *IEEE Trans. Geosci. Remote Sens.*, vol. 55, no. 3, pp. 1262–1272, Mar. 2017.

[12] M. D. Henschel, J. R. Buckley, and F. W. Dobson, "Estimates of wave height from low incidence angle sea clutter," in *Proc. 4th Int. Conf. Wave Hindcast. Forecast.*, Banff, AB, Canada, 1995.

[13] R. Gangeskar, "Wave height derived by texture analysis of X-band radar sea surface images," in *Proc. IEEE Int. Geosci. Remote Sens. Symp.*, vol. 7, Honolulu, HI, USA, 2000, pp. 2952–2959.

[14] H. Dankert, J. Horstmann, and W. Rosenthal, "Wind- and wave-field measurements using marine X-band radar-image sequences," *IEEE J. Ocean. Eng.*, vol. 30, no. 3, pp. 534–542, Jul. 2005.

[15] X. Liu, W. Huang, and E. W. Gill, "Wave height estimation from shipborne X-band nautical radar images," *J. Sensors*, vol. 2016, 2016, Art. no. 1078053.

[16] Z. Chen, Y. He, and B. Zhang, "An automatic algorithm to retrieve wave height from X-band marine radar image sequence," *IEEE Trans. Geosci. Remote Sens.*, vol. 55, no. 9, pp. 5084–5092, Sep. 2017.

[17] R. Vicen-Bueno, C. Lido-Muela, and J. Nieto-Borge, "Estimate of significant wave height from non-coherent marine radar images by multilayer perceptrons," *EURASIP J. Adv. Signal Process.*, vol. 2012, 2012, Art. no. 84.

[18] J. Park, K. Ahn, C. Oh, and Y. S. Chang, "Estimation of significant wave heights from X-band radar using artificial neural network," *J. Korean Soc. Coastal Ocean Engineers*, vol. 32, no. 6, pp. 561–568, 2020.

[19] H. Kim, K. Ahn, and C. Oh, "Estimation of significant wave heights from X-band radar based on ANN using CNN rainfall classifier," *J. Korean Soc. Coastal Ocean Engineers*, vol. 33, no. 3, pp. 101–109, 2021.

[20] L. Cornejo-Bueno, J. Nieto-Borge, E. Alexandre, K. Hessner, and S. Salcedo-Sanz, "Accurate estimation of significant wave height with support vector regression algorithms and marine radar images," *Coastal Eng.*, vol. 114, pp. 233–243, 2016.

[21] S. Salcedo-Sanz, J. Nieto-Borge, L. Carro-Calvo, L. Cuadra, K. Hessner, and E. Alexandre, "Significant wave height estimation using SVR algorithms and shadowing information from simulated and real measured X-band radar images of the sea surface," *Ocean Eng.*, vol. 101, no. 1, pp. 244–253, 2015.

[22] W. Duan, K. Yang, L. Huang, and X. Ma, "Numerical investigations on wave remote sensing from synthetic X-band radar sea clutter images by using deep convolutional neural networks," *Remote Sens.*, vol. 12, no. 7, 2020, Art. no. 1117.

[23] S. Bai, J. Z. Kolter, and V. Koltun, "An empirical evaluation of generic convolutional and recurrent networks for sequence modeling," 2018, *arXiv: 1803.01271*.

[24] X. Chen, W. Huang, C. Zhao, and Y. Tian, "Rain detection from X-band marine radar images: A support vector machine-based approach," *IEEE Trans. Geosci. Remote Sens.*, vol. 58, no. 3, pp. 2115–2123, Mar. 2020.

[25] X. Chen and W. Huang, "Identification of rain and low-backscatter regions in X-band marine radar images: An unsupervised approach," *IEEE Trans. Geosci. Remote Sens.*, vol. 58, no. 6, pp. 4225–4236, Jun. 2020.

[26] D. Stredulinsky and E. Thornhill, "Ship motion and wave radar data fusion for shipboard wave measurement," *J. Ship Res.*, vol. 55, no. 2, pp. 73–85, 2011.

[27] C. M. Senet, J. Seemann, and F. Ziemer, "The near-surface current velocity determined from image sequences of the sea surface," *IEEE Trans. Geosci. Remote Sens.*, vol. 39, no. 3, pp. 492–505, Mar. 2001.

[28] C. Shen, W. Huang, E. W. Gill, R. Carrasco, and J. Horstmann, "An algorithm for surface current retrieval from X-band marine radar images," *Remote Sens.*, vol. 7, no. 6, pp. 7753–7767, 2015.

[29] J. C. Nieto-Borge and C. Guedes-Soares, "Analysis of directional wave fields using X-band navigation radar," *Coastal Eng.*, vol. 40, no. 4, pp. 375–391, 2000.

[30] J. Nieto-Borge, K. Reichert, and K. Hessner, "Detection of spatio-temporal wave grouping properties by using temporal sequences of X-band radar images of the sea surface," *Ocean Modelling*, vol. 61, pp. 21–37, 2013.

[31] J. C. Nieto-Borge, G. R. RodrÍguez, K. Hessner, and P. I. González, "Inversion of marine radar images for surface wave analysis," *J. Atmos. Ocean. Technol.*, vol. 21, no. 8, pp. 1291–1300, 2004.

[32] N. E. Huang, Z. Wu, S. R. Long, K. C. Arnold, X. Chen, and K. Blank, "On instantaneous frequency," *Adv. Adaptive Data Anal.*, vol. 1, no. 2, pp. 177–229, 2009.

[33] Z. Yang, W. Huang, and X. Chen, "Evaluation and mitigation of rain effect on wave direction and period estimation from X-band marine radar images," *IEEE J. Sel. Topics Appl. Earth Obs. Remote Sens.*, vol. 14, pp. 5207–5219, 2021.
[34] R. M. Haralick, K. Shanmugam, and I. Dinstein, "Textural features for image classification," *IEEE Trans. Syst., Man, Cybern.*, vol. SMC- 3, no. 6, pp. 610–621, Nov. 1973.
[35] F. Yu and V. Koltun, "Multi-scale context aggregation by dilated convolutions," in *Proc. Int. Conf. Learn. Representations*, 2016, p.13.
[36] V. Nair and G. Hinton, "Rectified linear units improve restricted Boltzmann machines," in *Proc. Intl. Conf. Mach. Learn*., 2010, pp. 807–814.
[37] N. Srivastava, G. Hinton, A. Krizhevsky, I. Sutskever, and R. Salakhutdinov, "Dropout: A simple way to prevent neural networks from overfitting," *J. Mach. Learn. Res.*, vol. 15, no. 1, pp. 1929–1958, 2014.
[38] K. He, X. Zhang, S. Ren, and J. Sun, "Deep residual learning for image recognition," in *Proc. IEEE Comput. Soc. Conf. Comput. Vis. Pattern Recognit.*, 2016, pp. 770–778.
[39] D. Kingma and J. Ba, "Adam: A method for stochastic optimization," in *Proc. Int. Conf. Learn. Representations*, 2015, p.15.
[40] A. Smola and B. Schölkopf, "A tutorial on support vector regression," *Statist. Comput.*, vol. 14, pp. 199–222, 2004.
[41] J. Chung, C. Gulcehre, K. Cho, and Y. Bengio, "Empirical evaluation of gated recurrent neural networks on sequence modeling," *arXiv:1412.3555*.

Weimin Huang (Senior Member, IEEE) received the B.S., M.S., and Ph.D. degrees in radio physics from Wuhan University, Wuhan, China, in 1995, 1997, and 2001, respectively, and the M.Eng. degree in electrical engineering from the Memorial University of Newfoundland, St. John's, NL, Canada, in 2004.

From 2008 to 2010, he was a Design Engineer with Rutter Technologies, St. John's, NL, Canada. Since 2010, he has been with the Faculty of Engineering and Applied Science, Memorial University of Newfoundland, where he is currently a Professor. He has authored more than 250 research articles. His research interests include the mapping of oceanic surface parameters via high-frequency ground wave radar, X-band marine radar, and global navigation satellite systems.

Dr. Huang was the recipient of the Postdoctoral Fellowship from the Memorial University of Newfoundland, the Discovery Accelerator Supplements Award from the Natural Sciences and Engineering Research Council of Canada, in 2017, and the IEEE Geoscience and Remote Sensing Society 2019 Letters Prize Paper Award. He is also an Area Editor for the IEEE CANADIAN JOURNAL OF ELECTRICAL AND COMPUTER ENGINEERING, an Associate Editor for IEEE ACCESS, an Editorial Board Member of *Remote Sensing*, and a Guest Editor for IEEE JOURNAL OF SELECTED TOPICS IN APPLIED EARTH OBSERVATIONS AND REMOTE SENSING. He serves as a regular Reviewer over 60 international journals and a Reviewer for many IEEE international conferences, such as RadarCon, International Conference on Communications, IEEE Global Communications Conference, IEEE International Geoscience and Remote Sensing Symposium, and Oceans. He has been a Member of the Technical Program Committee. He has served as the Technical Program Co-Chair for the IEEE Newfoundland Electrical and Computer Engineering Conference, in 2012 and 2013.

Zhiding Yang (Student Member, IEEE) received the B.Eng. degree in electrical information engineering from the Wuhan University of Science and Technology, Wuhan, China, in 2018. He is currently working toward the M.Eng. degree in electrical engineering with the Memorial University of Newfoundland, St. John's, NL, Canada.

His research interest includes sea parameter estimation from X-band marine radar data.

Xinwei Chen (Student Member, IEEE) was born in Guangzhou, China. He received the B.Eng. degree in information engineering from the South China University of Technology, Guangzhou, China, in 2017, and the Ph.D. degree in electrical engineering from the Memorial University of Newfoundland, St. John's, NL, Canada, in 2021.

Since September 2021, he has been with the Vision and Image Processing Lab, University of Waterloo, Waterloo, ON, Canada, as a Postdoctoral Fellow.

His research interest includes X-band marine radar ocean surface remote sensing.